IEEE Access
Multidisciplinary | Rapid Review | Open Access Journal

Received 4 October 2022, accepted 15 October 2022, date of publication 19 October 2022, date of current version 26 October 2022.

Digital Object Identifier 10.1109/ACCESS.2022.3215959

RESEARCH ARTICLE

Design, Fabrication and Test of a High-Temperature Superconducting Linear Synchronous Motor Mover Magnet Prototype for High-Speed Maglev

DAOYU HU, YI ZHANG, AND KAI MAO
Institute of Magnetic Levitation and Electric Propulsion, Haidian, Beijing 100146, China
China Aerospace Science and Industry Corporation Ltd., Haidian, Beijing 100146, China

Corresponding author: Kai Mao (casicmk@163.com)

This work was supported in part by the Beijing Natural Science Foundation under Grant JQ20018, and in part by the National Natural Science Foundation of China through Youth Science Foundation Program under Grant 51907183.

ABSTRACT High-temperature superconducting linear synchronous motors (HTS-LSMs) have many advantages, such as high thrust density, high efficiency, large electromagnetic gap, and liquid-helium-free refrigeration, because of the high operating temperature and good mechanical tolerance of high-temperature superconductors. Therefore, HTS-LSMs have broad application prospects in the field of high-speed maglev propulsion system. To study the dynamic stability of an HTS-LSM, this work aims at designing, fabricating and testing an HTS magnet as the mover magnet of an HTS-LSM. The HTS mover magnet is a monopole HTS magnet, and it is designed according to electromagnetic, structural, and thermal properties and the measurement system. A thermal model and structural dynamics model were constructed to analyze the dynamic refrigeration performance and structural dynamics characteristics of the HTS magnet. The validation of these models was verified by experimental results. The HTS coils in the HTS mover magnet were fabricated using epoxy impregnation with primary and secondary curing processes. Static tests and dynamic tests were performed to comprehensively study the characteristics of the HTS magnet. The magnet could be cooled to below 20 K and could be excited to 246 A with a certain temperature margin. An electromagnetic simulator was designed and manufactured to realize the off-line simulation of the actual operation of the HTS-LSM. The dynamic experimental results show that the HTS magnet could withstand a vibration environment of up to 18 gRMS without quenching and structural damage. This study provides useful information for the design and application of an HTS-LSM.

INDEX TERMS Maglev, high-temperature superconducting linear synchronous motor (HTS-LSM), design, fabrication, test.

I. INTRODUCTION

High-speed railways such as CRH, TGV, ICE, Shinkansen, and KTX, are running worldwide providing people with convenience. With the development of society, people's demand for travel speed is getting higher and higher. To acquire faster speed (600+km/h), maglev train based on superconducting magnet technology is one of the high-speed maglev technology routes. Coated superconductors formed from the high-temperature superconducting (HTS) material $REBa_2Cu_3O_{7-\delta}$(REBCO) possess a high critical current and excellent mechanical tolerance to higher operating temperatures compared with low-temperature superconducting (LTS) materials for industrial applications. Most existing superconducting magnets employ Nb-Ti superconductors, which have a critical temperature of 9 K. Nb-Ti magnets therefore need to be cooled with liquid helium or 4 K cryocoolers. REBCO-coated conductors have a high transition temperature, and

The associate editor coordinating the review of this manuscript and approving it for publication was Giambattista Gruosso.

their current density in high magnetic field environments is superior to that of other superconductors. For example, the current density of REBCO-coated conductors at 40 K is almost the same as that of Nb-Ti conductors at 4 K [1]. A high operating temperature offers several advantages, namely, the magnets can be cooled by a cryocooler without liquid helium. Therefore, HTS magnets could overcome the limitation of liquid helium resources and provide a stronger magnetic field with lower cost. The applications of HTS magnets have attracted worldwide attention; HTS linear motors are one such application.

HTS linear motors can be divided into HTS linear synchronous motors (HTS-LSMs) and HTS linear induction motors (HTS-LIMs). Compared with the HTS-LIM, the HTS-LSM has higher thrust density and efficiency. Therefore, the HTS-LSM has more engineering and industrial application prospects. For instance, traction motors of high-speed and ultrahigh-speed maglev trains are an important application of the HTS-LSM. Japan is one of the first countries to develop superconducting maglev trains and has made numerous research achievements. To date, it has maintained a speed record of 603 km/h in the field of rail transit [2] using an LTS-LSM as the traction motor. The vibration and heat of the superconducting mover magnets caused by the harmonic magnetic field of the ground coils have been deeply studied by theoretical analysis, simulations and tests [3], [4], [5], [6]. Researchers have found that the quenching of mover magnets can be effectively prevented by reducing the harmonic magnetic field of the ground coils, improving the structural stiffness of the magnet and optimizing the materials for friction. In 2010, Japan began to study the feasibility of replacing the existing LTS magnets with HTS magnets. After confirming that fusion bonding is the best curing method for HTS coils [7], [8], Katsutoshi Mizuno manufactured and tested a real-scale REBCO coil, and the feasibility and dynamic stability of the REBCO coil were verified by excitation tests [9], mechanical vibration tests [10] and electromagnetic vibration tests [11]. More research on HTS magnets is in progress.

To increase the speed of existing wheel rail trains, the Korea Railroad Research Institute proposed a conceptual design of an HTS-LSM for a 600 km/h wheel-type railway. A prototype of the HTS-LSM was fabricated using second generation HTS wire, and static refrigeration and excitation tests and dynamic low speed propulsion tests were performed [12], [13], [14]. Moreover, the Korea Railroad Research Institute designed, fabricated and tested a subsonic HTS-LSM for the Hyperloop [15], which aims to accelerate to a velocity of 1200 km/h in a near-vacuum. Static propulsion tests and dynamic tests were performed to verify the proposed design models of the subsonic HTS-LSM. However, the maximum propulsion speed is only approximately 4 m/s [16].

China has also carried out basic research on HTS-LSMs for high-speed maglev. Guangtong Ma et al. studied the performance of a small-scale HTS-LSM with four mover air-core HTS mover coils in liquid nitrogen by simulation and experiment. A two-dimensional (2D) finite element model for calculating static electromagnetic characteristics and a three-dimensional (3D) finite element model for calculating dynamic electromagnetic characteristics were verified by the experimental results [17], [18]. Recently, the same group designed, fabricated and tested an HTS magnet for an electrodynamic suspension train. The magnet can be cooled to below 15 K and has been charged to 240 A without any mechanical damage or quenching observed [19]. However, only static tests were carried out, and there are no dynamic performance data reported. Zheng Huang et al proposed a design method for an on-board persistent-current superconducting magnet system with cooling-free operation, especially for superconducting maglevs [20], [21]. The structural dynamics of the HTS magnets were evaluated by simulation considering electromagnetic and thermal stress [22]. A double-layer short-pitch stator was chosen as the best stator structure for the HTS-LSM [23] and a test double-racetrack coil unit has been manufactured and investigated at 77 K [24]. Future bench tests will be performed at cryogenic temperatures with magnets energized at their rated current to investigate the dynamic performance of the HTS-LSM.

TABLE 1. Summary of Research Results on HTS-LSM Mover Magnet.

Research team	Country	Progress
Katsutoshi[7-11]	Japan	→1: 1 Prototype: 700kAt →Excitation test, mechanical vibration test and electromagnetic vibration test were successfully performed
Chang-Young Lee[12-14]	Korea	→Scaled prototype: 300kAt →Static refrigeration and excitation tests were successfully performed
Railroad Research Institute[16]	Korea	→Scaled prototype: 150kAt →Static refrigeration and excitation tests and dynamic low speed population (<5m/s) test were successfully performed
Guangtong Ma[17-18]	China	→Scaled prototype: 270kAt →Only static tests were performed
Zheng Huang[20-24]	China	Conceptual design & analysis
This paper	China	→Scaled prototype: 494kAt →Full process design of the magnet, new curing process, novel off-line simulation test method →Both static and dynamic tests (18 gRMS) were successfully performed

To summarize, there are few studies on the dynamic characteristics of superconducting mover magnets for HTS-LSMs, especially stability research under high vibration environments. In this study, a coated conductor unipolar magnet, which serves as an HTS-LSM mover, was systematically designed, fabricated and tested. A new epoxy impregnation method using Araldite MY750 epoxy resin was used to improve the thermal coupling of HTS coils. An internal and external pluggable copper current lead and an HTS current lead using BSCCO tapes were applied to reduce system heat

leakage. An electromagnetic simulator was used to simulate the harmonic magnetic field of the stator coils; thus, the dynamic characteristics of the HTS-LSM could be studied by off-line experimental simulation. Table 1 lists the summary and comparison of the research results on HTS-LSM mover magnet.

This paper is organized as follows. Section II presents the design, fabrication and performance analysis of the HTS magnet, including the overall structures, HTS coils, HTS persistent current switch (PCS), current leads and measurement system. Section III introduces the design and fabrication of the electromagnetic simulator. Section IV presents the static test results of the magnet, including the refrigeration test, excitation test and closed-loop test. Section V presents the dynamic test results of the magnet based on the electromagnetic simulator, including the sweep frequency test and electromagnetic vibration test, followed by the conclusions in Section VI.

II. DESIGN, FABRICATION AND ANALYSIS OF THE HTS MAGNET

A. OVERVIEW OF THE HTS MAGNET

Figure 1(a) and Figure 1(b) show 3D overviews of the HTS mover magnet of the HTS-LSM. The magnet is unipolar, and its electromagnetic design will be introduced next. The overall structural layout can be described as follows.

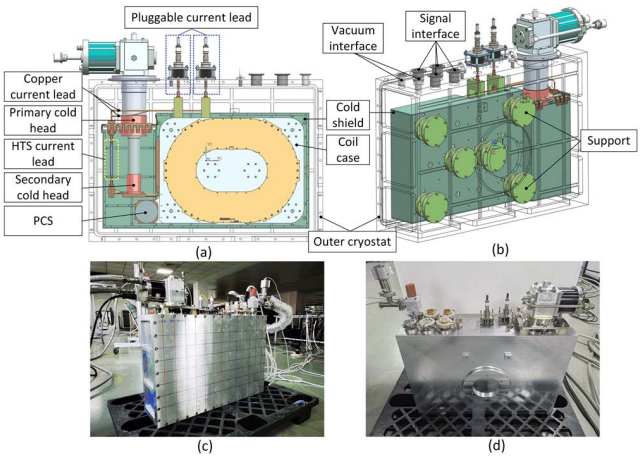

FIGURE 1. Overview of the HTS magnet. (a) 3D front view; (b) 3D axis view; (c) & (d) photographs.

(i) The cryocooler cold heads are located on the left of the coil case. The primary cold head of the cryocooler cools the cold shield through distributed cooling belts. The secondary cold head of the cryocooler cools the coil case through a centralized cooling belt. The model of the cryocooler is RDK-415D produced by Sumitomo Corporation. (ii) HTS coils are first wound on nonmetallic frameworks, cured with epoxy resin, and then assembled and cured again into a metal shell, i.e., the coil case. The PCS is fixed at the lower left corner of the coil case. The material of the coil case is Al 7075-T5. (iii) The coil case is connected with one side of the outer cryostat through six support rods. The middle part of the support rod is connected to the cold shield. Therefore, the coil case is supported by a unilateral cantilever structure. The material of the outer cryostat is Al 6061-T6. The material of the support rods is glass fiber reinforced polymer (GFRP). The material of the cold shield is Al 6061-T6. (iv) The cold shield wraps the six sides of the coil case. The cold shield and the outer cryostat are removable on one side, which is convenient for maintenance. (v) The current leads consist of three parts. From the high-temperature end to the low-temperature end, there are pluggable current leads, copper current leads and HTS current leads. The bottom fixed ends of the pluggable current leads are fixed with the coil case through GFRP. (vi) The vacuum interfaces and signal interfaces are located on the top side of the outer cryostat. Figure 1(c) and Figure 1(d) show photographs of the magnet.

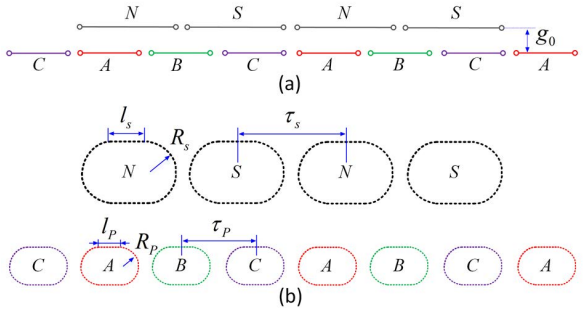

FIGURE 2. Electromagnetic topology of the HTS-LSM. (a) Pole-slot matching diagram; (b) dimension diagram.

TABLE 2. Key Design Parameters of The HTS-LSM.

Parameter	Specification
Motor	
Motor type	LSM
Number of phases	Double three-phase
Number of poles	4
Pole distance/τ_s	480 mm
Electromagnetic gap/g_0	111.5 mm
Stator coils	
Conductor material	Copper litz wire
Winding form	Single layer centralized winding
Arc segment radius/R_P	77.5 mm
Straight line length/l_P	70 mm
Coil spacing/τ_p	320 mm
Coil turns/N_p	20
Mover coils	
Conductor	0.20 mm×5.8 mm REBCO tape
Arc segment radius/R_s	130 mm
Straight line length/l_s	100 mm
Coil spacing/ τ_s	480 mm
Coil turns/N_s	2010 (335×6)
Rated current	246 A @ 30 K
Coil type	6 single pancake coils connected in series
Gap between pancakes	3 mm

B. HTS MOVER COIL

Figure 2 shows the electromagnetic topology of the target HTS-SLM. The pole-slot matching of the motor is three slots

and two poles, i.e., two mover coils or three stator coils can be placed in the same length. The mover coils and stator coils are both racetrack shaped. There are four motor poles, and there are three motor phases. Therefore, the motor can be regarded as a dual three-phase motor. The motor pole distance τ_s and electromagnetic gap g_0 are 480 mm and 111.5 mm, respectively. The stator coils are single layer centralized windings made of copper litz wires. The copper litz wires used can reduce eddy current losses of the stator coils. The spacing of the stator coils is $2\tau_s/3$, i.e., 320 mm. The number of stator coil turns N_p is 20. The mover coils are made of REBCO tape. The tape thickness is 0.19 mm. The tape widths before and after encapsulation were 4.8 mm and 5.8 mm, respectively. The turn-to-turn insulation is 25 μm polytetrafluoroethylene (PTFE) tape. The PTFE tape is wound together with the HTS tape. The winding tension of the HTS tape is 50 N. Because the PTFE tape is very soft, it is wound without tension. The mover coil magnetomotive force is 494.5 kAt. Each mover coil consists of six single pancake HTS coils connected in series. The gap between the single pancakes is 3 mm. Table 2 lists the detailed parameters of the HTS-LSM.

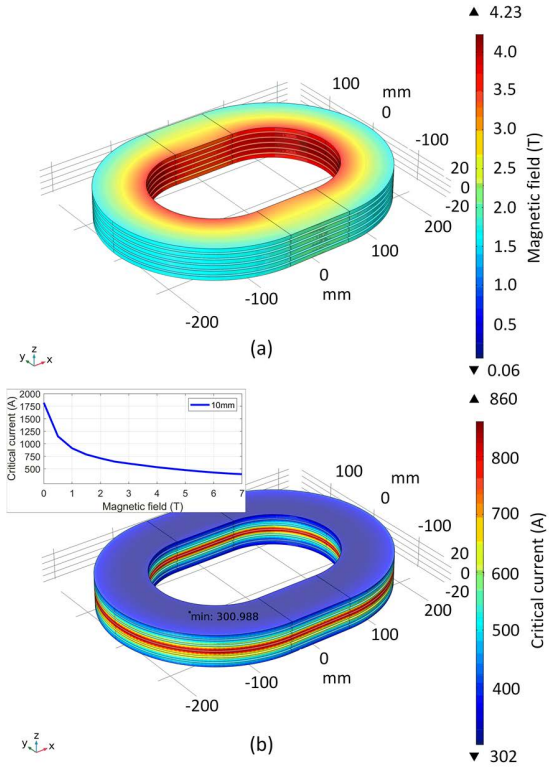

FIGURE 3. Electromagnetic characteristics of the HTS magnet. (a) Magnetic field distribution; (b) critical current calculation.

To reduce the difficulty and cost of research and development, a magnet with only one HTS mover coil was designed, fabricated and tested. Based on the research and development of the single mover coil magnet, relevant technical risks can gradually be determined. Figure 3(a) shows the magnetic field distribution of the HTS magnet with a single mover coil. The maximum magnetic field is 4.23 T, and the internal magnetic field is higher than the external magnetic field. The critical current is a key parameter for an HTS magnet. In this study, the critical current of the HTS magnet was calculated by a numerical approximation method: (i) The spatial magnetic field distribution is obtained by energizing the HTS magnet from a small current to a large current. (ii) Based on the attenuation characteristics of the critical current of HTS tapes under a magnetic field, the critical current distribution can be calculated. If the minimum calculated critical current is equal to the excitation current, the excitation current is determined to be the maximum allowable current of the HTS magnet, i.e., the excitation current is the critical current of the HTS magnet. Figure 3(b) shows the calculated critical current distribution of the HTS magnet excited with 300 A at 30 K. As shown in Figure 3(b), the minimum calculated critical current is 300.988 A, and thus, the critical current of the HTS magnet is approximately 300 A at 30 K. Therefore, the load factor of the HTS magnet is approximately 0.82 with a rated excitation current of 246 A at 30 K.

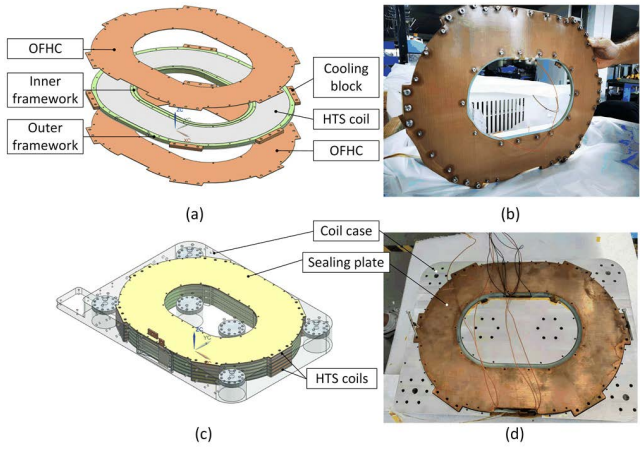

FIGURE 4. Fabrication of HTS coils. (a) Composition of an HTS coil; (b) picture of an HTS coil before curing; (c) assembly drawing of HTS coils and coil case; (d) picture of the coil case before curing.

The HTS magnet is cooled by conduction. This means that HTS coils in the HTS magnet are directly connected to heat transfer elements. Because of the influence of electromagnetic force, the HTS magnet serving as the mover of the HTS-LSM used in dynamic environments inevitably vibrates. To improve the thermal coupling of HTS coils, HTS coils and heat transfer elements must be tightly assembled and joined together. Katsutoshi Mizuno proposed two feasible methods, i.e., epoxy impregnation (Emerson & Cuming, Stycast 1266) [7] and fusion bonding (thermoplastic resin) [8], to manufacture HTS coils strongly coupled to cooling elements without performance degradation according to static experimental tests. In this study, a new epoxy impregnation method is proposed. Figure 4(a) shows the composition diagram of an HTS coil. The HTS coil has two

types of coil frameworks: an inner framework and an outer framework. The inner framework is used for coil winding, and the outer framework is used to control the epoxy resin pouring space. The material of the frameworks is G10. Two oxygen-free high-conductivity copper (OFHC) plates are installed on the top and bottom of the HTS coil to cool the HTS coil. Cooling blocks are used to connect the two OFHC plates. The HTS magnet consists of six HTS coils. Before assembly, each HTS coil was cured using Araldite MY750 epoxy resin. Figure 4(b) shows a picture of an assembled HTS coil before curing. The critical currents before and after curing of each HTS coil were measured in liquid nitrogen, and no degradation phenomenon was observed. Then, the six HTS coils were assembled into the coil case, as shown in Figure 4(c). Figure 4(d) shows a picture of the assembled coil case before curing. The assembled coil case was cured again using the same epoxy resin. The critical currents before and after curing of the coil case were also measured in liquid nitrogen, and no degradation phenomenon was observed. The feasibility of the curing method was thus verified.

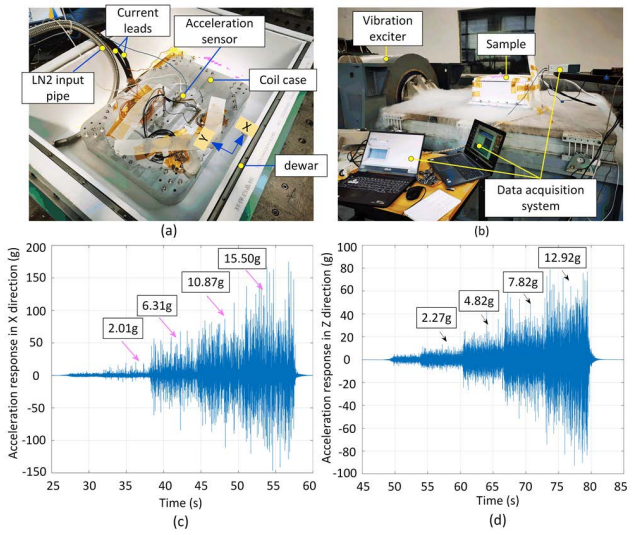

FIGURE 5. Mechanical vibration tests of the assembled coil case. (a) & (b) Pictures of the vibration tests; (c) acceleration response in the X direction; (d) acceleration response in the Z direction.

Moreover, a mechanical vibration test was performed after the coil case cured. The coil case was mechanically vibrated in a liquid nitrogen environment with a load factor of 70%. The vibration mode is random vibration. The random vibration spectrum type is a flat spectrum with a frequency range from 10 Hz to 1100 Hz. The maximum input vibration magnitude is 15 gRMS. In actual operation, the input vibration magnitude was loaded in four steps. The vibration test was performed in the X-, Y-, and Z-direction in sequence. Figure 5(a) and Figure 5(b) show pictures of the vibration test. Figure 5(c) and Figure 5(d) show the measured acceleration response during the X-direction and Z-direction vibration tests, respectively, and the RMS values of each step are marked. After the X-direction vibration test, the coil case was directly used to perform the Y-direction vibration test without changing the fixed direction of the uniaxial acceleration sensor. Therefore, the measured acceleration response is not the real acceleration response in the Y-direction and thus is not shown in Figure 5. The difference between the maximum acceleration response value and the maximum input acceleration value was caused by the control error of the vibration exciter. There is no quenching during these vibration tests. Therefore, the dynamic thermal stability of the assembled coil case manufactured by the proposed method was confirmed, and the coil case was deemed ready for general assembly with the HTS magnet.

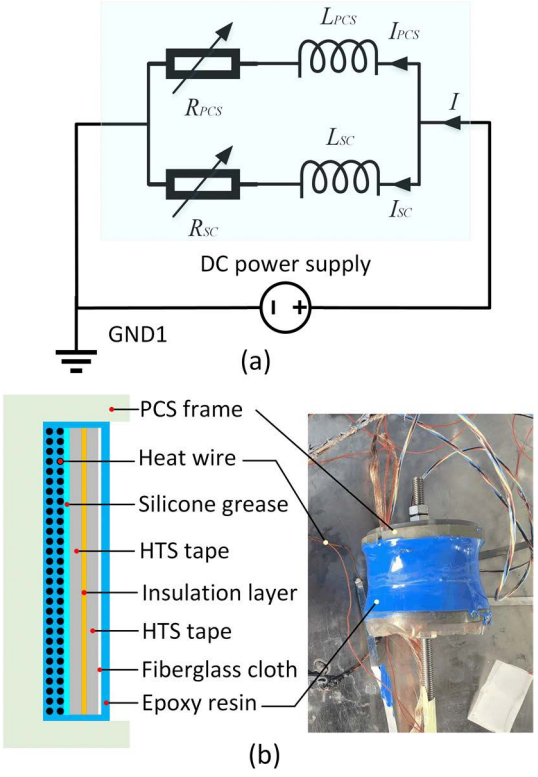

FIGURE 6. HTS PCS. (a) Equivalent circuit of the closed HTS magnet with a PCS; (b) composition diagram of the PCS.

C. HTS PCS

A PCS is used to close the HTS magnet. The normal-state resistance of the PCS should be large enough with its bypass current less than 10% of the HTS coil [25]. Figure 6(a) shows the equivalent circuit of the closed HTS magnet with a PCS. The HTS-coated conductor of the PCS is the same as that of the HTS coils. I_{PCS} and I_{SC} represent the currents in the PCS and HTS coils, respectively. L_{PCS} and L_{SC} represent the inductances of the PCS and HTS coils, respectively. R_{PCS} and R_{SC} represent the resistances of the PCS and HTS coils, respectively. Because the HTS coils are in a superconducting state, R_{SC} is equal to zero. Therefore, the current in the PCS is determined by the R_{PCS} and L_{PCS}. To reduce I_{PCS}, it is best to reduce L_{PCS}. In this study, a noninductive manufacturing

method was used for the PCS; thus, the L_{PCS} is also equal to zero. For this magnet system, the I_{PCS} is limited to less than 5 A; thus, the minimum required R_{PCS} can be calculated by the voltage U_{PCS} across the magnet at an average ramping rate of 0.025 A/s, as expressed by equation (1). Based on the copper resistivity at 110 K, the calculated length of the PCS is approximately 1300 mm.

$$R_{PCS} \geq \frac{U_{PCS}}{I_{PCS}} = \frac{\alpha L_{SC}}{I_{PCS}} \approx 7.6\ \text{m}\Omega \tag{1}$$

Figure 6(b) shows the composition diagram and a picture of the PCS. Its fabrication process is as follows: (i) Manganin heating wires were wound on the PCS frame made of GFRP, and then thermally conductive silicone grease was daubed on the outermost layer of the heating wires. (ii) Two HTS tapes were wound in parallel to form a solenoid. An insulator layer was used for the turn-to-turn insulation of the two HTS tapes. The two tapes at one end were directly soldered together, and the two tape at the other end were soldered with the HTS coils. (iii) A fiberglass cloth was used to fasten the components. (iv) Finally, the PCS was cured using Stycast 2850 epoxy resin at room temperature. Table 3 lists the key design parameters of the PCS.

TABLE 3. Key design parameters of the PCS.

Parameter	Value
HTS tape dimension	0.20 mm×5.8 mm REBCO tape (with 50 μm copper encapsulation)
HTS tape length	1300 mm
Winding method	Non inductive winding
PCS frame	GFRP
Heat wire	Manganin wire (0.2 mm)
Resistance of heat wire	480 Ω@293 K, 330 Ω@77 K
Silicone grease	Apiezon N
Insulation layer	PTFE
Epoxy resin	Stycast 2850

D. CURRENT LEAD

Figure 7 shows the composition of the current lead of the HTS magnet. It consists of three types of current leads: copper pluggable current leads, copper current leads and HTS current leads. The pluggable current leads are used to cut off heat conduction from the external excitation equipment to the magnet. The copper current leads are used to connect the HTS current leads and the pluggable current leads. A common and well-studied method was used to design the copper current leads. Using the design method proposed in [26], the sectional area and length of the copper current leads are 40 mm^2 and 360 mm, respectively. HTS current leads are used to reduce heat leakage.

Table 4 lists some key parameters of the HTS current leads. The tape used is the first generation (1G) HTS BSCCO tape. The width and thickness are 4.3 mm and 0.23 mm, respectively. Six BSCCO tapes are soldered in parallel to increase the current carrying capacity. The length of each tape is 120 mm. The ends of the HTS current leads are connected to the primary and secondary cold heads of the cryocooler, as shown in Figure 1(a). Figure 8 shows the lift factor of the BSCCO tape and the magnetic field distribution on the HTS current leads with the HTS magnet rated excitation. As shown in Figure 8, the maximum magnetic field is 0.72 T. The maximum magnetic field is the composite magnetic field of the perpendicular and parallel magnetic fields. In general, the critical current of BSCCO tape attenuates more in the perpendicular field than in the parallel field. To improve the design margin, the maximum magnetic field is regarded as the maximum perpendicular field to evaluate the corresponding critical current of the HTS tape. Based on the lift factor curves of the BSCCO tape under the applied perpendicular field, the critical current of a single tape at 66 K is approximately 52.02 A (i.e., 180 A × 1.7× 0.17, where 1.7 is the temperature coefficient and 0.17 is the magnetic field coefficient). Thus, the critical current of the HTS current lead is 312.12 A (i.e., 52.02 A × 6) at 66 K. Therefore, the

TABLE 4. Key design parameters of the HTS current leads.

Parameter	Value
HTS tape type	1G-HTS, BSCCO tape
HTS tape width	4.3 mm±0.2 mm
HTS tape thickness	0.23 mm±0.01 mm
Critical current	180 A@77 K, self-field
Number of HTS tapes	Six tapes in parallel
Length of each tape	120 mm

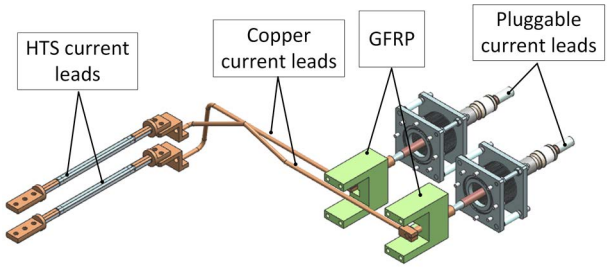

FIGURE 7. Current lead of the HTS magnet.

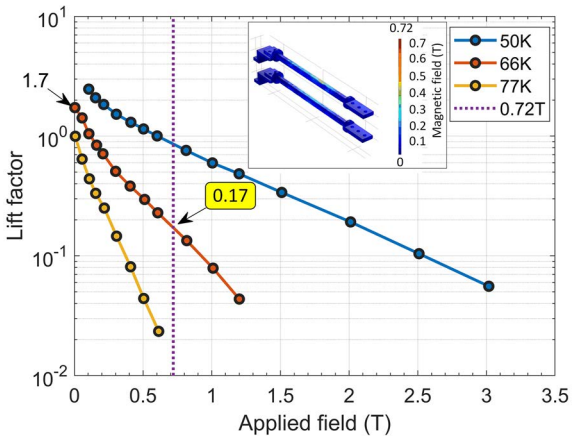

FIGURE 8. Current lead of the HTS magnet.

HTS current lead could operate safely at 66 K and still have a certain temperature margin.

E. MEASURE SYSTEM DESIGN

To fully understand the state of the magnet during tests, different types of sensors are mounted on the HTS magnet, as shown in Figure 9. The vibration sensors are mounted on the coil case (A1∼A6), the cold head (A7) and the outer cryostat (A8). All of the vibration sensors are uniaxial vibration sensors, and A1∼A8 are used to measure the acceleration response in the Z-direction. This is because the Z-direction acceleration response of the magnet is the largest under the action of electromagnetic force. The CernoxTM temperature sensors are mounted on the secondary cold head (C1), the PCS (C2) and the coil case (C3∼C6). It should be noted that temperature sensor C5 is inside the coil case. The PT-100 temperature sensors are mounted on the primary cold head (P1), the high-temperature end (P2) and the cold shield (P3∼P6, P5′). P3∼P6 are on the same side of the cold shield, and P5′ is on the opposite cold shield with the same location as P5.

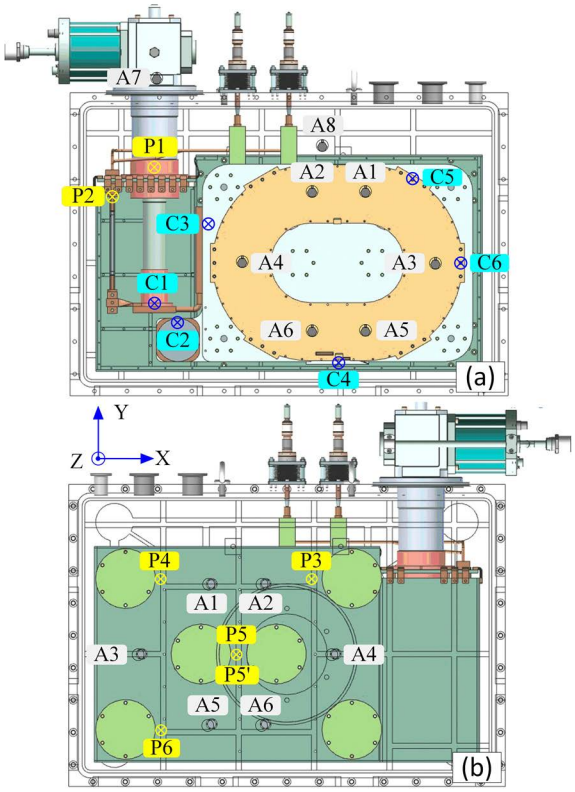

FIGURE 9. Sensor layout.

F. THERMAL AND STRUCTURAL DYNAMIC ANALYSIS

Thermal performance and structural dynamics performance are two key properties for the mover magnet of the HTS-LSM. Thermal performance demonstrates the quality of the magnet thermal design and effectiveness of the refrigeration system. The structural dynamics performance characterizes the acceleration response of the magnet under the action of the electromagnetic force, which provides a method to formulate the assessment criterion for the vibration adaptability of each component of the magnet. Next, finite element methods are presented that analyze these two typical performances, i.e., refrigeration performance under static operation and structural dynamics performance under dynamic operation.

Figure 10 shows the simulated temperature distributions on the cold head, HTS current leads, coil case, HTS coils, cold shields and support rods under extreme refrigeration conditions. Extreme refrigeration means that the magnet is cooled with pluggable current leads disconnected, the PCS is not heated, and the magnet is not excited. Therefore, the magnet system has the lowest heat leakage and can be cooled to the lowest temperature. As shown in Figure 10, we obtained the following information: (i) The highest temperature of the primary cold head was 37.5 K, and the lowest temperature of the secondary cold head was 6.85 K. The lowest temperature of the coil case was 7.88 K, and it was at the connection between the coil case and the secondary cold head. Therefore, the heat exchange temperature difference between the secondary cold head and the coil case was 1.03 K. (ii) The temperatures at the high-temperature end and low-temperature end of the HTS current leads were approximately 35 K and 10 K, respectively. Because the critical temperature of the HTS current leads was higher than 66 K, as estimated in Part 2.4, the HTS current leads have a sufficient temperature margin.

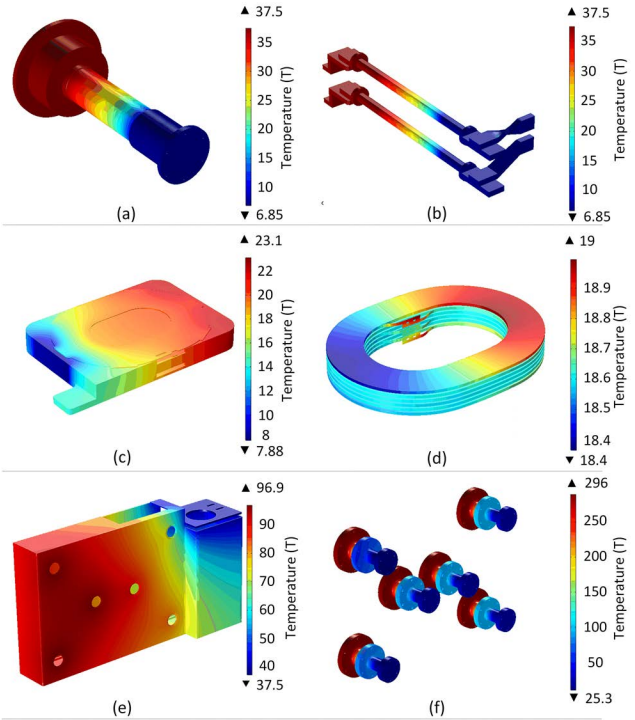

FIGURE 10. Simulated temperature distribution. (a) Cold heads; (b) HTS current leads; (c) coil case; (d) HTS coils; (e) cold shield; (f) support rods.

(iii) The highest temperature of HTS coils was 19.0 K with a temperature difference of 0.6 K. (iv) For cold shields, the temperature near the cold head was low, and the temperature away from the cold head was high. The highest temperature was 96.9 K. Figure 11 shows the temperature curves of several points marked in Figure 9 during the extreme refrigeration process. As shown in Figure 11, the cooling rate of the primary cooling head was the fastest, followed by the cold shield, and the HTS coil and coil case are the slowest. It took approximately six hours to cool the primary head to the minimum temperature. It took approximately 37.5 h and 38.0 h to cool the HTS coil and secondary cold head to the minimum temperature, respectively.

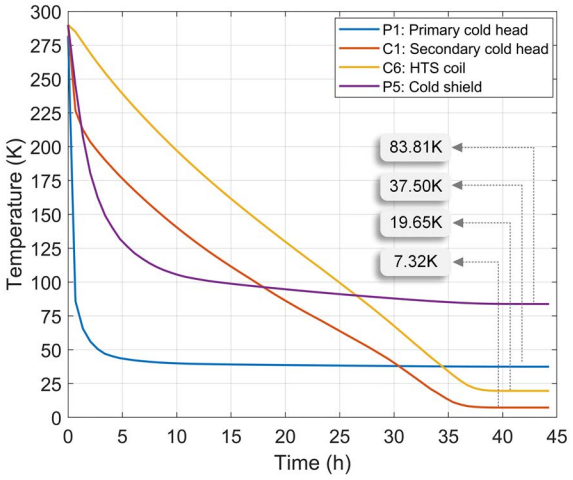

FIGURE 11. Temperature curves of several key points (P1: primary cold head, C1: secondary cold head, C6: HTS coil, P5: cold shield).

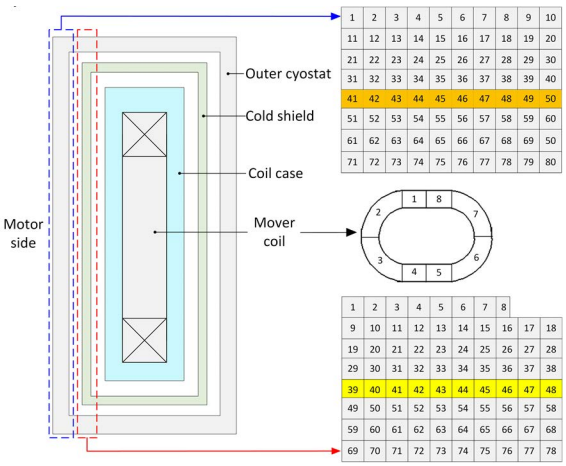

FIGURE 12. Blocking methods of the outer cryostat, the cold shield and the mover coil for electromagnetic force calculation.

For the HTS-LSM, its structural dynamics represent the vibration acceleration response characteristics of structural components under electromagnetic force. Therefore, the loading of electromagnetic force in the structural dynamics model is very important. To improve the calculation accuracy of the model, a block extraction method was used to calculate the electromagnetic force. Moreover, because of the shielding effect of the metal outer cryostat and the cold shield between the stator and the mover, there are electromagnetic forces on the outer cryostat and the cold shield caused by electromagnetic harmonics (except for the electromagnetic force on the HTS coil, which is caused by the fundamental magnetic field). Figure 12 shows the blocking methods for the outer cryostat, the cold shield and the mover coil for electromagnetic force calculation; only the shielding effects of the outer cryostat and cold shield on the motor side were considered. The outer cryostat is divided into 80 blocks, and the cold shield is divided into 78 blocks. The mover coil is divided into 8 blocks, and each line segment and arc segment are divided into two blocks.

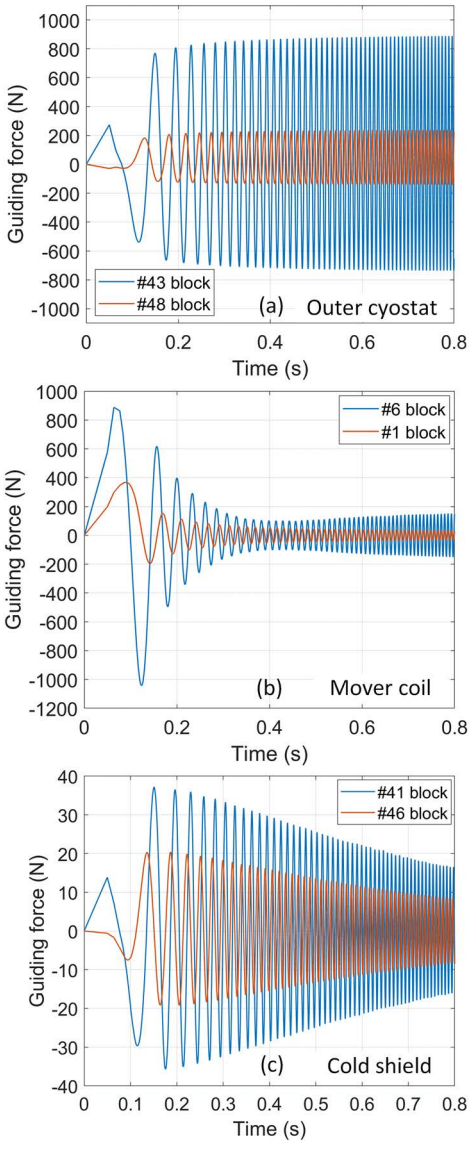

FIGURE 13. Typical electromagnetic force curves in the time domain of the blocks in the (a) outer cryostat, (b) mover coil and (c) cold shield.

Figure 13(a)~Figure 13(c) show the variation curves of the guiding electromagnetic force in the time domain of the

blocks in the outer cryostat, the mover coil and the cold shield, respectively. Two blocks are selected from each component, i.e., the 43rd and 48th blocks of the outer cryostat, the 1st and 6th blocks of the mover coil, and the 41st and 46th blocks of the cold shield. In the calculation, the HTS-LSM accelerates to 400 km/h on a 235 m long test line, the HTS magnet was rated excited with 246 A and the stator coils were excited with 1050 A peak current. Only the electromagnetic forces in the first 0.8 s are shown. Moreover, the influence of temperature on the distribution of electromagnetic force is considered based on thermal analysis. As seen in Figure 13, the electromagnetic forces on different blocks of the same component are highly dynamic, while their phases and amplitudes are different. Moreover, the frequency of these forces increases with time, and the magnitude of these forces also varies with time. The force on the outer cryostat increases gradually with the frequency, while the forces on the cold shield and the mover coil decrease gradually. This is because the shielding effect of the outer cryostat on the harmonic magnetic field increases gradually with frequency. Figure 14(a) shows the time domain variation of the guiding electromagnetic forces of the 41st to 50th blocks of the outer cryostat, and Figure 14(b) shows the time domain variation of the guiding electromagnetic forces of the 39th to 48th blocks of the cold shield. As shown in Figure 14, the electromagnetic force distributions on the outer cryostat and the cold shield have the following characteristics: (i) The electromagnetic force distributions on the outer cryostat and the cold shield are similar. Because the main component of the stator space harmonic magnetic field is the second harmonic in space, there are two significant peaks at any time. (ii) The amplitude of the electromagnetic force on the outer cryostat is much greater than that on the cold shield. This is because most of the harmonic magnetic field has been shielded by the outer cryostat, and the harmonic magnetic field penetrating the outer cryostat is small. In summary, it is necessary to extract the electromagnetic force by blocks for highly accurate structural dynamics analysis.

Figure 15(a) and Figure 15(b) show the acceleration response in the time domain and in the frequency domain, respectively, of points A1∼A6 marked in Figure 9. As shown in Figure 15(a), there are several acceleration response peaks, and the corresponding acceleration response amplitudes increase with time. The maximum acceleration response is approximately 80 m/s^2. As shown in Figure 15(b), the power spectral density (PSD) roughly increases with frequency, and the corresponding frequencies of several typical peaks are 53.7 Hz, 73.2 Hz, 181.6 Hz and 325.2 Hz.

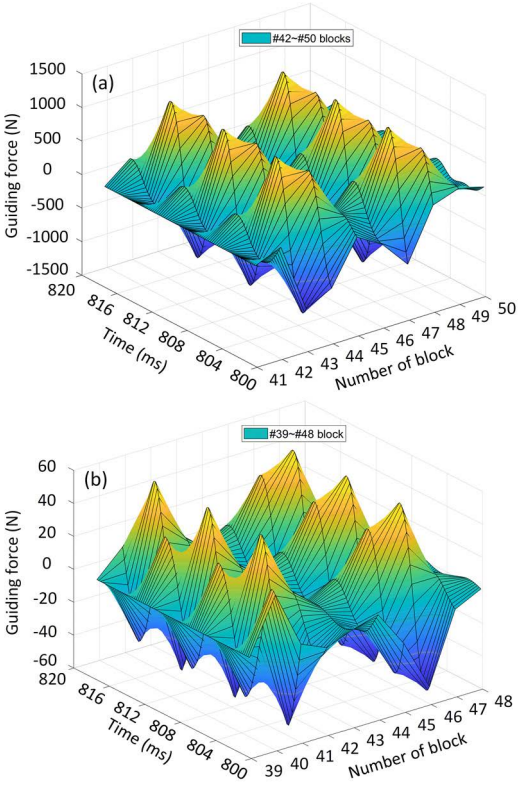

FIGURE 14. Electromagnetic force distribution of blocks (a) #41∼#50 in the outer cryostat and (b) #39∼#48 in the cold shield.

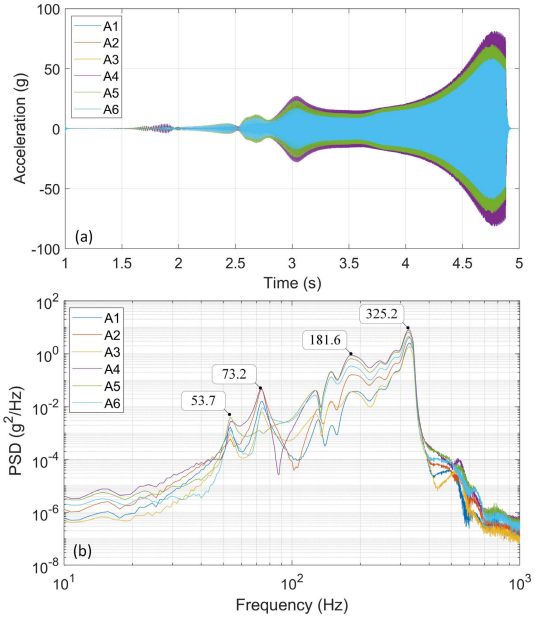

FIGURE 15. Acceleration response in the (a) time domain and (b) frequency domain.

III. DESIGN AND FABRICATION OF THE ELECTROMAGNETIC SIMULATOR

For an HTS-LSM, the thrust and structural performance of the motor are generally assessed through a static locked rotor test. However, the static locked rotor test could not assess the dynamic performance of an HTS-LSM motor under dynamic operating conditions. Under the action of electromagnetic force, the motor will inevitably vibrate. The vibration will lead to relative movement between components of the HTS mover magnet, and thus friction heat will

be produced. Friction heat is an important factor for HTS mover magnet quenching under dynamic operation. Therefore, it is necessary to construct a test condition to simulate the dynamic operation of the HTS-LSM to study the dynamic adaptability of the HTS mover magnet. In this section, we propose an off-line experimental simulation method to simulate the dynamic operation of the HTS-LSM.

A. DESIGN PROCESS

For the designed HTS-LSM, the fundamental magnetic field of the stator coils is synchronized with the DC magnetic field of the mover coils. The interaction of the fundamental magnetic field and the DC magnetic field produces steady-state thrust and normal force and will not cause motor vibration. However, the harmonic magnetic field of the stator coils is not synchronized with the DC magnetic field of the mover coils. The interaction of the harmonic magnetic field and the DC magnetic field causes motor vibration. Therefore, the off-line experimental simulation method could only simulate the interaction of the harmonic magnetic field and the DC magnetic field for studying the structural dynamics. This can greatly reduce the complexity of the design and fabrication of the electromagnetic simulator.

Figure 16 shows the Fourier analysis of the stator magnetic field of two test lines on the mover coil. One test line is the centerline of the mover coil, as illustrated in Figure 16(a), and the other test line is above the centerline of the mover coil, as illustrated in Figure 16(b). The horizontal and vertical coordinates represent the harmonic order and the harmonic ratio, respectively. The harmonic ratio is the ratio of the harmonic magnetic field value and the fundamental magnetic field value. As shown in Figure 16(a) and Figure 16(b), the main component of the harmonic magnetic field is the second harmonic magnetic field in space, and its corresponding harmonic ratio is greater than or equal to 0.70. Therefore, the electromagnetic simulator was designed to mainly simulate the second harmonic magnetic field of the stator coils for simplicity.

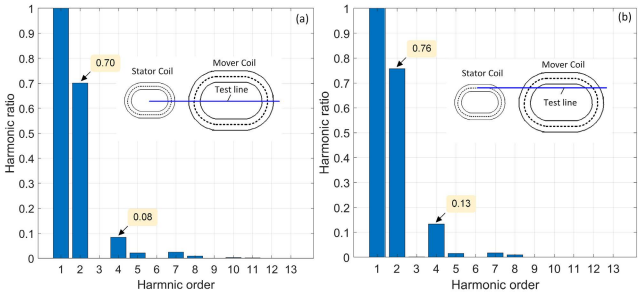

FIGURE 16. Fourier analysis of the stator magnetic field (a) of the centerline and (b) above the centerline of the mover coil.

The core component of the electromagnetic simulator is the excitation coils used to generate the second harmonic magnetic field. Figure 17(a)~Figure 17(c) show the electromagnetic topology, phase sequence and parameter definition of the excitation coils, respectively. A double layer excitation coil structure was adopted to reduce the additional harmonic magnetic field generated by the electromagnetic simulator itself. The polar distance of the excitation coils is equal to the motor polar distance τ_s, and the distance between adjacent coils is $\tau_s/3$, as shown in Figure 17(a). The excitation coils are excited with three phases, and the phase sequence and the phase angle are shown in Figure 17(b). Figure 17(c) shows the parameter definition of the excitation coils, and the corresponding dimension parameters are listed in Table 5. The material of the excitation coils is copper litz wire to reduce the eddy current loss. The coils on layer #1 and layer #2 have 14 and 19 turns, respectively. The layer #1 coils are located near the mover coil side. The heights of the layer #1 coils and the layer #2 coils (H_1 & H_2) are both 168 mm. The lengths of the layer #1 coils and the layer #2 coils (L_1 & L_2) are 256 mm and 238 mm, respectively. The radii of the layer #1 coils and the layer #2 coils (R_1 & R_2) are both 84 mm. The distance between the layer #1 coils and the layer #2 coils (d_{12}) is 13 mm.

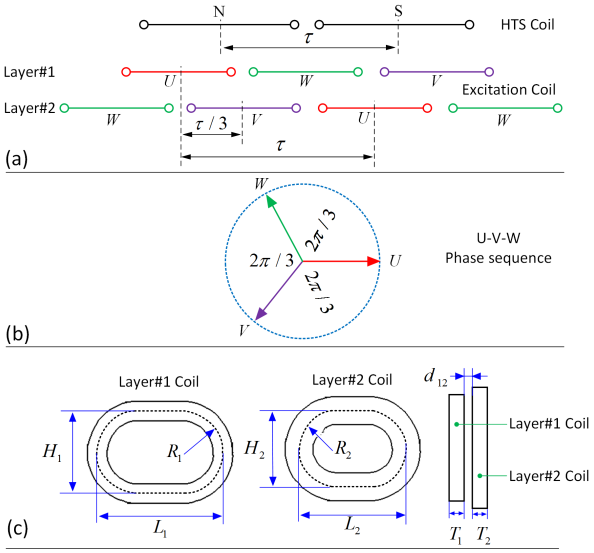

FIGURE 17. Electromagnetic simulator. (a) Layout of the excitation coils with two layers; (b) phase sequence and phase angle of the excitation coils; (c) drawing of the key dimensions of the excitation coils.

TABLE 5. Key design parameters of the electromagnetic simulator.

Parameter	Value
Phase number	3
Polar distance	480 mm
Turns of layer #1 coil	14
Number of layer #1 coils	9
Turns of layer #2 coil	19
Number of layer #2 coils	9
Conductor material	Copper litz wire
Cross section of single turn conductor	3 mm×20 mm
H_1/H_2	168 mm/168 mm
L_1/L_2	256 mm/238 mm
R_1/R_2	84 mm/84 mm
d_{12}	13 mm

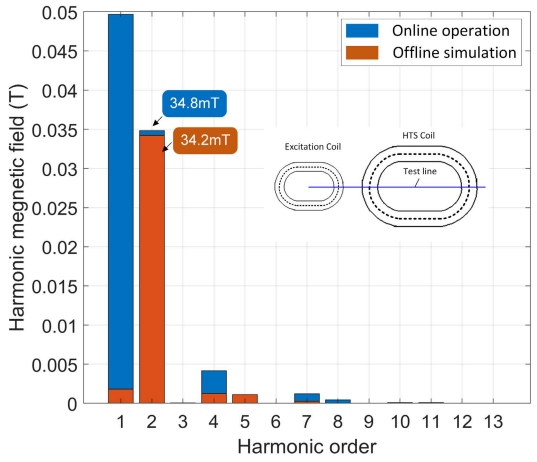

FIGURE 18. Comparison of the harmonic magnetic field generated by the HTS-LSM and the electromagnetic simulator.

B. VERIFICATION

To verify the effectiveness of the above designed electromagnetic simulator, the harmonic magnetic field and electromagnetic force generated by the HTS-LSM and the electromagnetic simulator, i.e., generated by the online operation and by the offline simulation, are compared. Figure 18 shows the comparison of the harmonic magnetic field generated by online operation and offline simulation. As shown in Figure 18, the second harmonic magnetic fields of the online operation and offline simulation are 34.8 mT and 34.2 mT, respectively. The relative error is only 1.72%. Moreover, the magnitude of the harmonic magnetic field, except for the second harmonic magnetic field generated by the excitation coils, is very small.

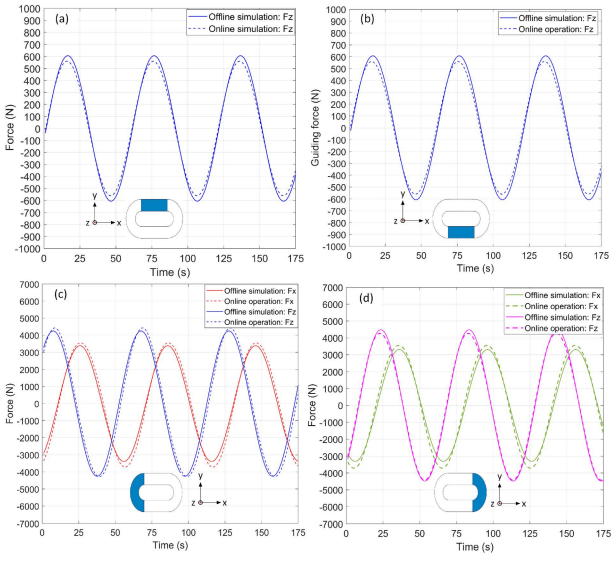

FIGURE 19. Comparison of the electromagnetic force generated by the HTS-LSM and the electromagnetic simulator. (a) & (b) Electromagnetic force in straight line segments; (c) & (d) electromagnetic force in circular arc segments.

Figure 19(a)∼Figure 19(d) show comparisons of the electromagnetic force generated by the HTS-LSM and the electromagnetic simulator in the upper straight-line segment, lower straight-line segment, left arc segment and right arc segment of the HTS mover coil. The electromagnetic force in straight line segments is only the guiding force (F_z), while the electromagnetic force in arc segments consists of both the propulsion force (F_x) and guiding force (F_z). As shown in Figure 19, the electromagnetic force in different segments generated by the designed electromagnetic simulator fit well with those generated by the HTS-LSM. Therefore, the effectiveness of the designed electromagnetic simulator has been proven based on the recurrence results of the harmonic magnetic field and electromagnetic force on the HTS mover coil.

IV. STATIC TESTS OF THE MAGNET

A. REFRIGERATION TESTS

Static tests consist of refrigeration tests, closed loop tests and excitation tests. First, an extreme refrigeration test was performed. Figure 20(a) and Figure 20(b) show the experimental temperature curves of points C1∼C6 and points P1∼P6, respectively, as marked in Figure 9. As the partially enlarged drawing in Figure 20(a) shows, it takes approximately 39.0 h

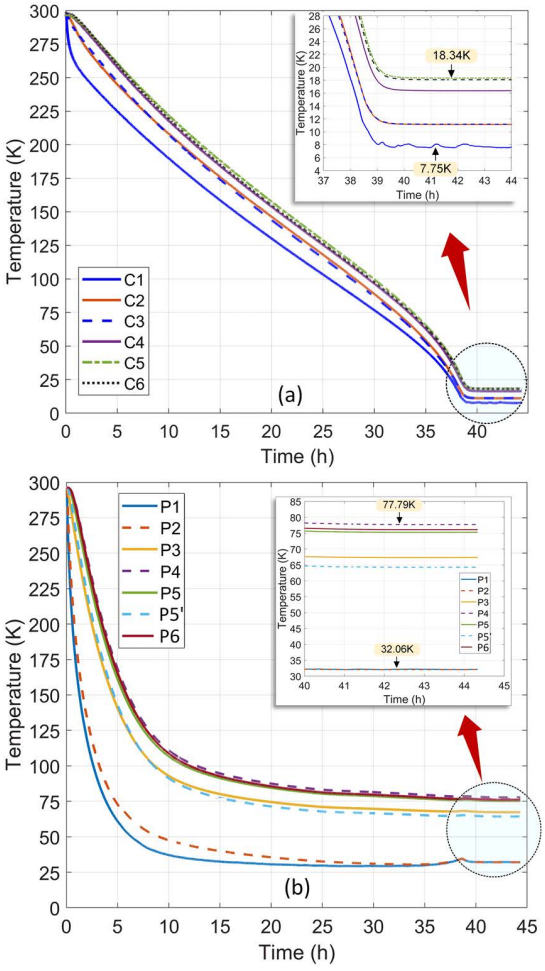

FIGURE 20. Results of the extreme refrigeration test. (a) Temperature curves of points C1∼C6; (b) temperature curves of points P1∼P6.

to cool points C1∼C6 to the minimum temperature, and the lowest temperatures of point C1 and point C6 are 7.75 K and 18.34 K, respectively. The calculated cooling time, lowest temperature of point C1 and lowest temperature of point C6 as described in Part F of Section II are 38.0 h, 7.32 K and 19.65 K, respectively.

As the partially enlarged drawing in Figure 20(b) shows, the lowest temperatures of points P1 and P5 are 32.06 K and 77.79 K, respectively. The calculated lowest temperatures of point P1 and point P5 are 37.5 K and 83.81 K, respectively, as described in Part F of Section II. The calculated temperature in the low temperature zone is in good agreement with the measured results, and the maximum difference is no more than 1.31 K, while the calculated temperature in the high-temperature zone is quite different from the measured results, in which the temperature difference of the cold shield reaches as high as 6.02 K. The calculation error may be caused by neglecting the contact thermal resistance between components. The calculation accuracy of the established thermal model needs to be further improved.

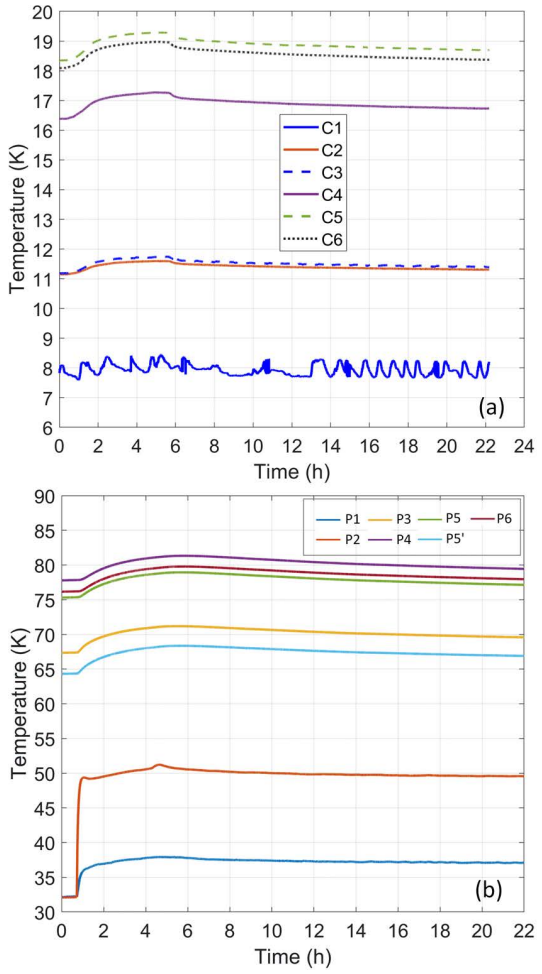

FIGURE 21. Results of pluggable current leads connected after the extreme refrigeration test. (a) Temperature curves of points C1∼C6; (b) temperature curves of points P1∼P6.

Following the extreme refrigeration test, pluggable current leads were connected, and their influence on the magnet temperature rise was studied. Figure 21(a) and Figure 21(b) show the curves of temperature variation of points C1-C6 and points P1∼P6, respectively. As shown in Figure 21(a), the temperature of points C1∼C6 increases first and then decreases and finally tends to be stable after the pluggable current leads are connected. The temperature rise of points C1∼C6 did not exceed 0.5 K. As shown in Figure 21(b), the temperature of points P1∼P6 also increases first and then decreases and finally tends to be stable after the pluggable current leads are connected. The rise in temperature of point P2 occurs significantly faster than that of other points because point P2 is directly connected to the pluggable current leads. Moreover, the temperature rise of point P2 is also significantly higher than that of the other points. The temperature rise of point P2 is approximately 18 K, while that of other points is not more than 5 K. In summary, the connection of pluggable current leads has a greater impact on the temperature rise of the primary refrigeration components (including primary cooling head, cold shield, high temperature terminal of HTS current lead) and a smaller impact on the temperature rise of the components connected to the secondary cooling head (including secondary cooling head, coil case, HTS coils and PCS).

After the pluggable current leads are connected, the stable temperature of each point is within the safe temperature range, and the temperature rise while closing the PCS is then tested. Figure 22(a) and Figure 22(b) show the curves of temperature variation of points C1-C6 and points P1∼P6, respectively. As shown in Figure 22 (a), the maximum temperature of the PCS exceeds 92 K, indicating that the PCS was successfully opened. The temperature rise of point C1 and points C3∼C6 is approximately 6 K. The maximum temperature of points C3∼C6 does not exceed 26 K. As shown in Figure 22 (b), all of the temperature increases of points P1∼P6 are not larger than 2 K, and the stable maximum temperature of point P2 is not larger than 55 K. Because the critical temperature of the HTS mover coil is greater than 30 K, as described in Part B of Section II, and the allowable working temperature of the high-temperature end of the HTS current lead is higher than 66 K, as described in Part D of Section II, the HTS magnet has a temperature margin for excitation tests. For safety, a low-level excitation test was carried out before the rated excitation test.

B. LOW-LEVEL EXCITATION TESTS

For the HTS mover magnet, additional heat sources, including Joule heating of copper current leads, Joule heating of superconducting joints and AC loss in excitation, will further increase its temperature. Therefore, a low-level excitation test was carried out first for safety at an excitation current of 125 A. Figure 23(a) and Figure 23(b) show the curves of temperature variation of points C1-C6 and points P1∼P6, respectively, in the low-level excitation test. As shown in Figure 23(a), the temperature rise of point C1 and points

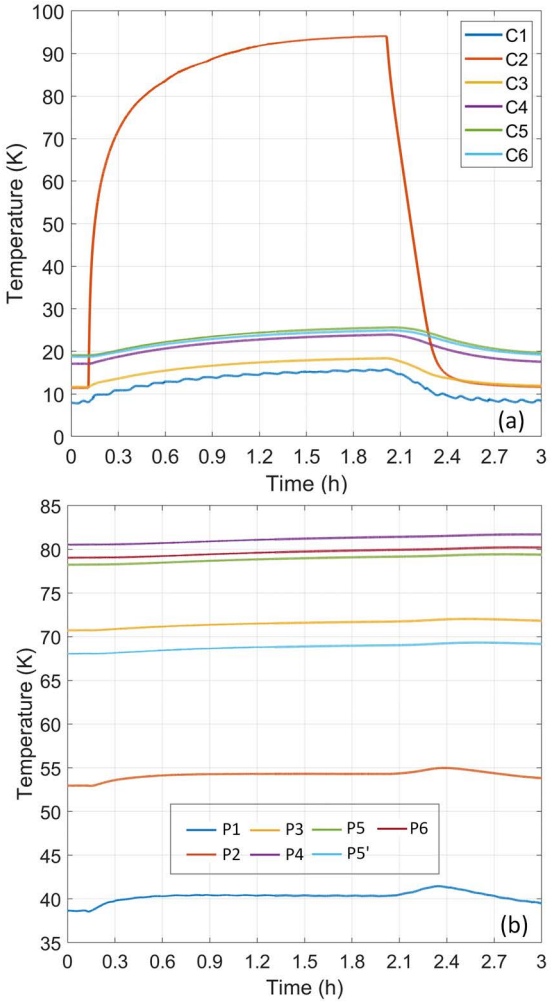

FIGURE 22. Results of closing the PCS after connecting the pluggable current leads. (a) Temperature curves of points C1∼C6; (b) temperature curves of points P1∼P6.

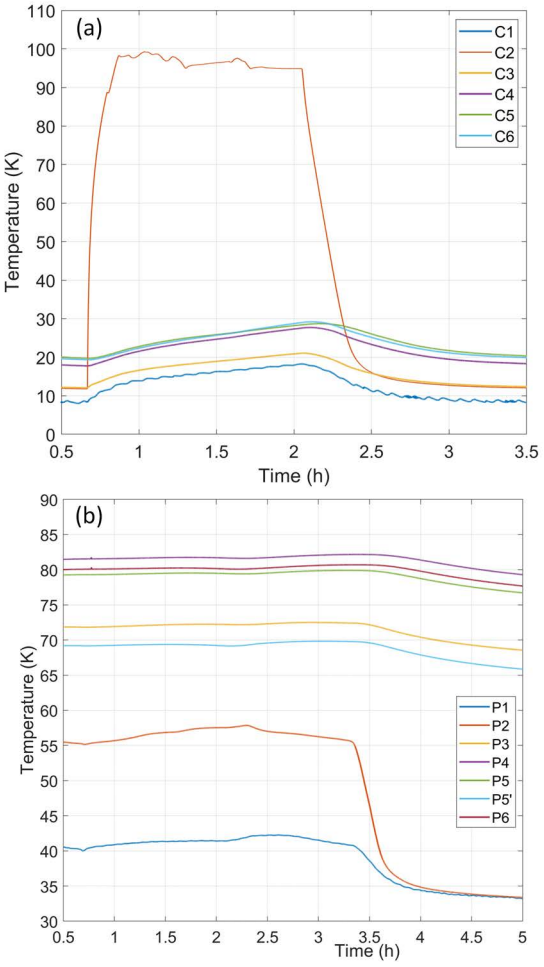

FIGURE 23. Results of the low-level excitation test. (a) Temperature curves of points C1∼C6; (b) temperature curves of points P1∼P6.

C3∼C6 is approximately 10 K, and the maximum temperature of points C3∼C6 is approximately 30 K. It is inferred that if the excitation continues to the rated current of 246 A, the maximum temperature of the HTS mover coil might exceed 40 K. It is very likely to exceed the critical current temperature of the HTS mover coil and cause the HTS magnet to quench. Therefore, the PCS was removed in the following rated excitation test and dynamic test. As shown in Figure 23(b), the temperature rise of points P1∼P6 is not larger than 3 K, and the maximum temperature of the high-temperature terminal of the HTS current lead is approximately 58 K, which is smaller than 66 K.

C. RATED EXCITATION TESTS

The cooling path of the coil case is optimized to improve the temperature uniformity and temperature margin of the HTS mover coil before the rated excitation test. Figure 24 shows a picture of the cooling path optimization of the coil case. Four newly added copper cooling belts are led from the secondary

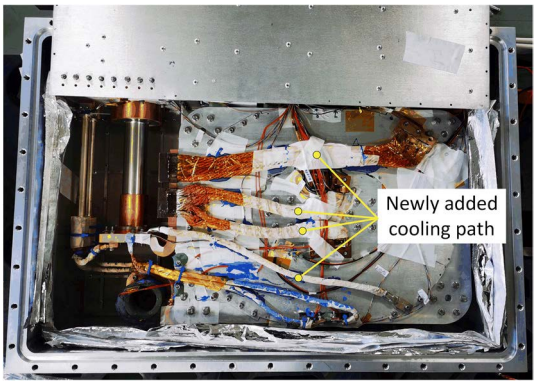

FIGURE 24. Cooling path optimization of the coil case.

cooling head to the far end of the coil case. Moreover, the hot connection between C2 point and the secondary cold head was also cut off.

Figure 25 shows the comparison of the measured temperature of points C1∼C6 before and after the cooling path optimization. The measured temperatures of points C1∼C6 before (and after) the cooling path optimization are 7.75 K

(7.90 K), 11.18 K (14.09 K), 11.18 K (11.37 K), 16.37 K (15.14 K), 18.34 K (16.77 K), and 18.07 K (15.00 K), respectively. The reason for the temperature increase at C1 and C3 points is that the conduction heat leakage at C1 and C3 points increases caused by the newly added cooling path. The reason for the temperature increase at C2 point is that the hot connection between C2 point and the secondary cold heat is cut off. The maximum temperatures of points C1∼C6 before and after optimization are 18.34 K and 16.77 K, respectively. The cooling path optimization reduces the maximum temperature by 1.57 K. Moreover, the maximum temperature difference between points C1∼C6 before and after optimization is 10.59 K and 8.87 K, respectively. The cooling path optimization improves the uniformity of the temperature distribution and reduces the maximum temperature of the HTS mover coil.

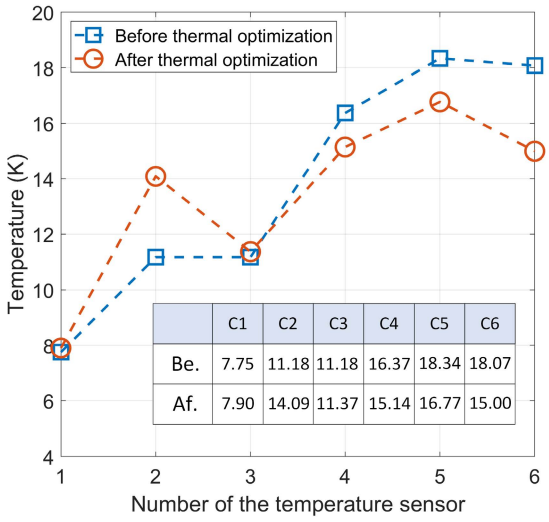

	C1	C2	C3	C4	C5	C6
Be.	7.75	11.18	11.18	16.37	18.34	18.07
Af.	7.90	14.09	11.37	15.14	16.77	15.00

FIGURE 25. Comparison of the temperature of points C1∼C6 before and after cooling path optimization.

Next, the rated excitation test was performed. Figure 26(a) shows the curves of the measured magnetic field and each HTS single pancake coil voltage during the rated excitation. VCoil*i* (i=1, 2, …, 6) represents the voltage of the six HTS single pancake coils stacked from top to bottom. The excitation time is approximately 2 hours. The magnetic field and voltage remain stable after excitation, which indicates that there is no quenching. Moreover, the voltages of the six HTS single pancake coils are basically coincident, and there is considerable high-level noise in the voltage signal. The real-time voltage signal cannot be directly used as the criterion of the magnet quenching. Figure 26(b) shows the curves of the temperature variation of points C1-C6 during the rated excitation test. As shown in Figure 26(b), the temperature of point C5 is the highest because the temperature sensor is installed into the mover coil. The maximum temperature and temperature rise of point C5 is not greater than 23 K and approximately 6 K, respectively.

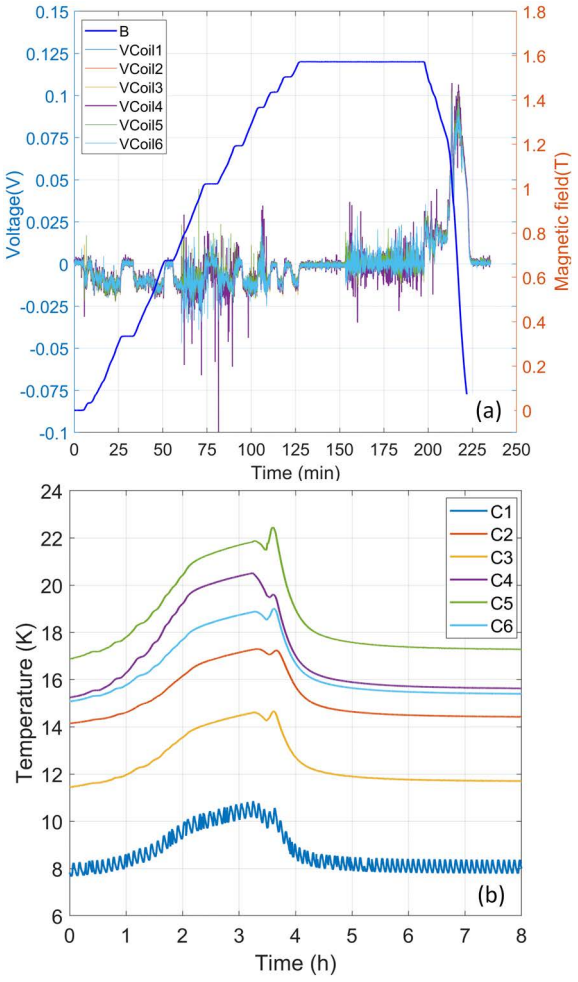

FIGURE 26. Results of the rated excitation test. (a) Curves of the magnetic field and HTS coil voltage during rated excitation; (b) temperature curves of points C1∼C6.

V. DYNAMIC TESTS OF THE HTS MAGNET

A. TEST CONDICTIONS AND PROCESS

Dynamic tests were performed after static tests. Dynamic tests include sweep frequency tests and simulated operation tests using an electromagnetic simulator. Figure 27(a) and Figure 27(b) show the global view and side view of the off-line test platform, respectively. The excitation module consisting of the excitation coils and their supporting structures was installed on the sidewall of a support beam. The support beam is made of concrete with nonmagnetic reinforcement. The HTS magnet was installed on the sidewall of a fixed device. The material of the fixed device was also nonmagnetic. The excitation module and the HTS magnet were arranged face to face. A converter system was used to supply AC current with variable frequency and amplitude for the excitation coils. The HTS magnet was in the open-loop state during dynamic tests, i.e., the excitation power supply was not disconnected, and the PCS was not heated. Moreover, the cryocooler was in operation during these dynamic tests.

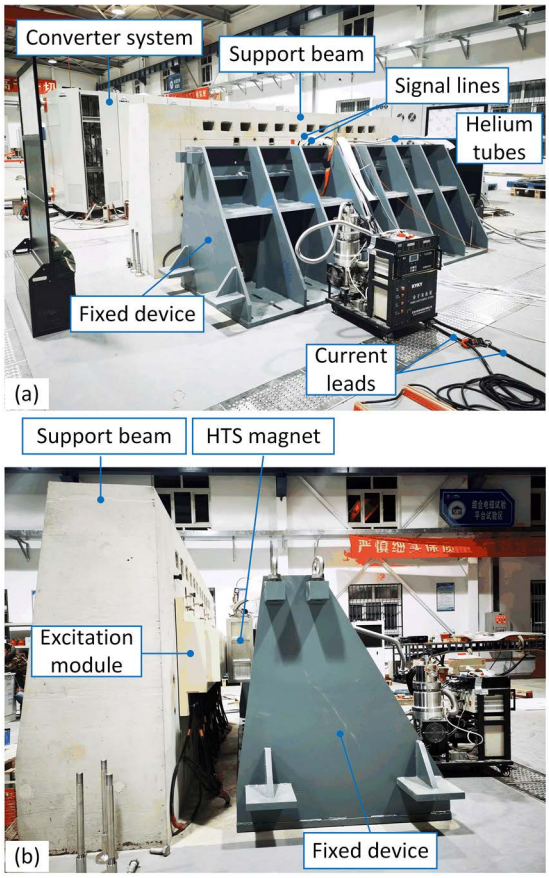

FIGURE 27. Pictures of the electromagnetic simulator. (a) Global view; (b) side view.

B. RESULTS AND DISCUSSION

A sweep frequency test was first carried out to obtain the basic structure information of the HTS magnet. The HTS magnet was excited to 100 A by a DC power source, and the excitation coils were supplied with an AC current by the convert system. The amplitude of the AC current is 100 A. The sweep frequency range of the AC current is 0 Hz ∼ 350 Hz, and the sweep time is approximately 20 seconds. Figure 28 shows the PSD of the acceleration response of points A1∼A6, as marked in Figure 9, during the sweep frequency test. Each PSD peak represents a structural model of the HTS magnet. As shown in Figure 28, typical modal frequencies of the HTS magnet include 50.0 Hz, 79.1 Hz, 222.2 Hz, 310.8 Hz, and 429.8 Hz.

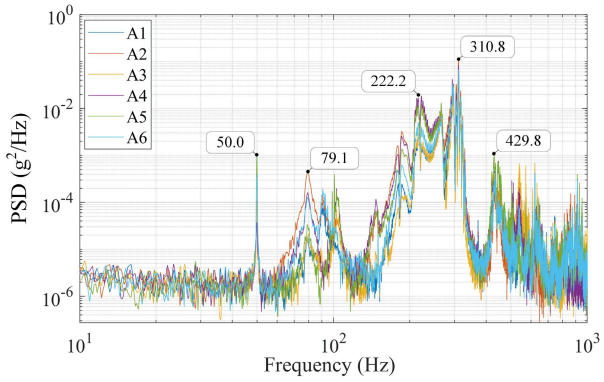

FIGURE 28. PSD of the acceleration response of points A1∼A6 during the sweep frequency test.

Figure 29 shows the acceleration response of points A1∼A6 in the time domain. It can be seen from the inset image in Figure 29 that there is no phase difference in the acceleration response of each measuring point, which indicates that the case structure is rigid and does not bend or twist. Figure 30 shows the time-frequency diagram of the acceleration response of point A1. There are many frequency doubling signals in the acceleration response, including $3f_0$, $6f_0$, $9f_0$, and $12f_0$. f_0 is the fundamental frequency of the HTS-LSM. The triple frequency signal strength is the strongest, and the twelve-octave frequency is the weakest. As shown in Figure 30, the electromagnetic simulator can generate 2nd, 4th, 5th, 7th, 8th, 10th, 11th, and 13th harmonic magnetic fields in space. The 2nd and 4th harmonic magnetic fields in space generate the 3rd harmonic magnetic field in the time domain, the 5th and 7th harmonic magnetic fields in space generate the 6th harmonic magnetic field in the time domain, the 8th and 10th harmonic magnetic fields in space generate the 9th harmonic magnetic field in the time domain, and the 11th and 13th harmonic magnetic fields in space generate the 12th harmonic magnetic field in the time domain. The frequency with the strongest intensity in the triple frequency signal is 310.8 Hz, which is consistent with the PSD analysis in Figure 28. Notably, there is a 50 Hz fixed frequency signal, which is the first-order modal frequency of the fixed device, as shown in Figure 27.

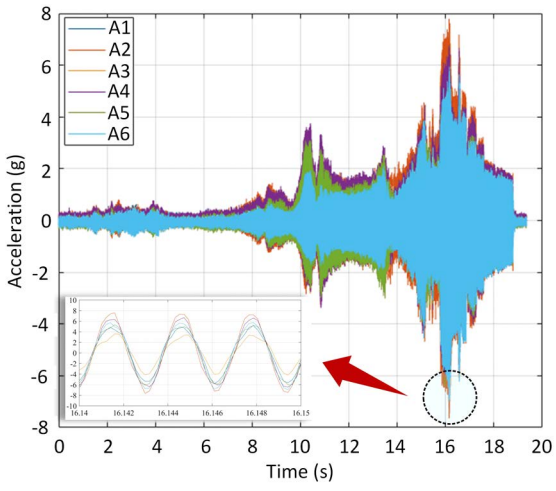

FIGURE 29. Acceleration response in the time domain of points A1∼A6 during the sweep frequency test.

A simulated operation test was performed after the sweep frequency test, which was used to simulate the harmonic magnetic field and electromagnetic force on the HTS mover magnet when the HTS-LSM accelerated to 400 km/h on a test line with a length of 235 m. The HTS magnet was excited to

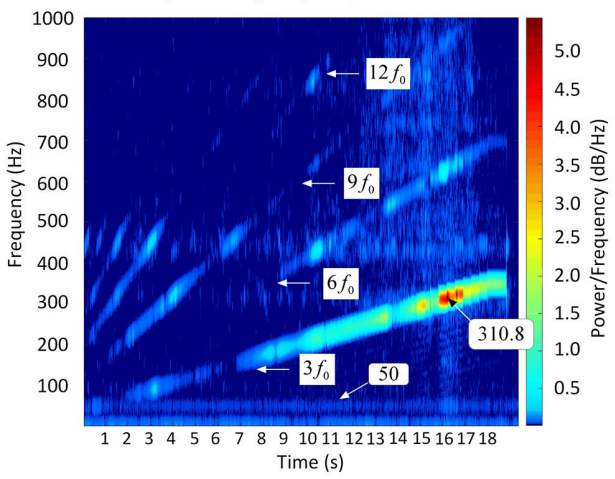

FIGURE 30. Time-frequency diagram of the sweep frequency test.

the rated current of 246 A, and the stator coils were supplied with 1050 A peak three-phase currents. The excitation coils were supplied with current according to equations (2) ∼ (3) based on the design principle described in Section III.

$$if\ t \le t_0,\ \begin{cases} i_U = 0 \\ i_V = I_{\max} \sin\left(\frac{2\pi}{3}\right) t/t_0 \\ i_W = I_{\max} \sin\left(\frac{4\pi}{3}\right) t/t_0 \end{cases} \tag{2}$$

$$if\ t_0 < t \le t_1,\ \begin{cases} i_U = I_{\max} \sin\left(\frac{3\pi}{2\tau} \cdot a \cdot (t-t_0)^2\right) \\ i_V = I_{\max} \sin\left(\frac{3\pi}{2\tau} \cdot a \cdot (t-t_0)^2 + \frac{2\pi}{3}\right) \\ i_W = I_{\max} \sin\left(\frac{3\pi}{2\tau} \cdot a \cdot (t-t_0)^2 + \frac{4\pi}{3}\right) \end{cases} \tag{3}$$

where i_U, i_V and i_W are the three-phase currents of the excitation coils; $I_{\max}$ is a constant, and its value is 635 A; and t_0 is the three-phase current loading time in ramp mode, which prevents quenching due to sudden current loading. During the actual operation of the HTS-LSM, t_0 is taken as 100 ms; t_1 is the time taken for the HTS-LSM to accelerate to 400 km/h on the 235 m long test line; a is the average acceleration of the HTS-LSM accelerating to 400 km/h on the 235 m test line, and a= $v/(t_1\text{-}t_0)$; and τ is the pole distance of the HTS-LSM, and its value is 0.48 m.

Figure 31 shows the PSD of the acceleration response of points A1∼A6, as marked in Figure 9, during the simulated operation test. The typical modal frequencies of the HTS magnet are basically consistent with the measured results of the sweep frequency test, which indicates that there is no structural damage to the HTS magnet. Figure 32(a) and Figure 32(b) show the acceleration response of points A1∼A6 and their corresponding RMS values, respectively. As shown in Figure 32(a), the maximum acceleration response peak value is approximately 80 g, and the

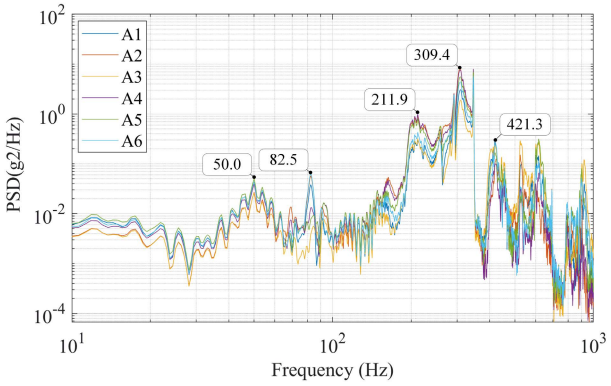

FIGURE 31. PSD of the acceleration response of points A1∼A6 during the simulation operation test.

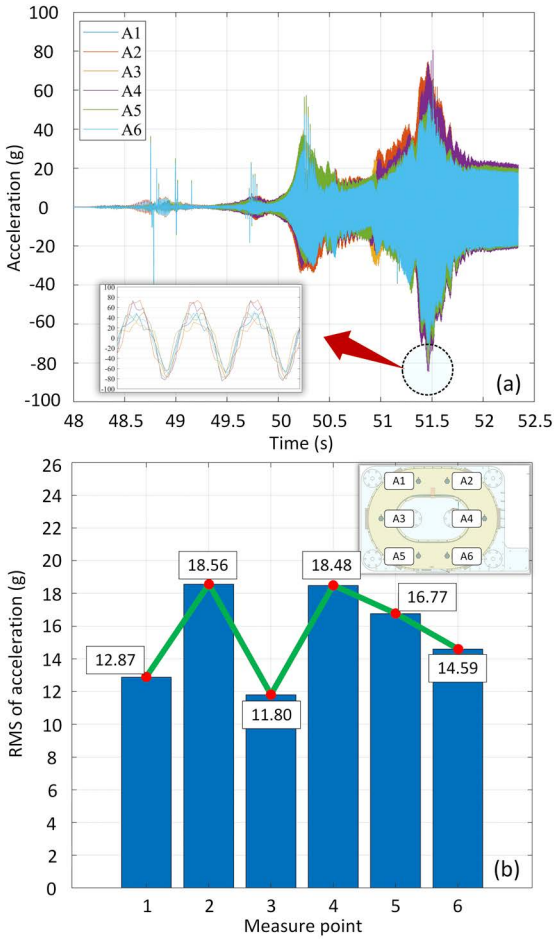

FIGURE 32. Acceleration response of points A1∼A6 during the simulation operation test. (a) Time domain curves; (b) RMS values.

acceleration response phase of each measuring point remains consistent. This shows that the coil case and the HTS mover coil are still not bent or twisted under a high-level vibration environment. Therefore, the structure of the HTS magnet is relatively rigid, which can suppress the frictional heat caused by the relative displacement between components under a vibrating environment. As shown in Figure 32(b), the

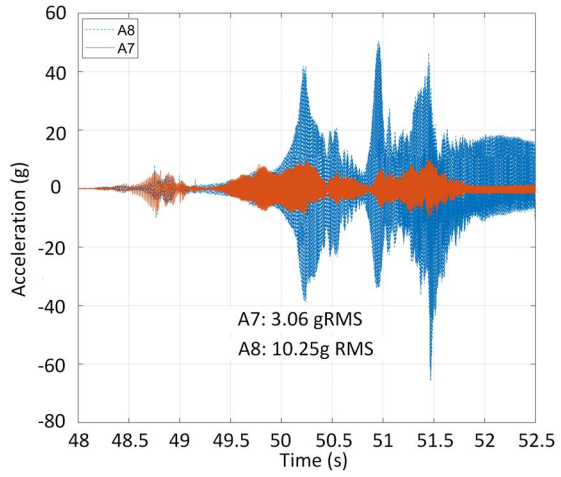

FIGURE 33. Acceleration response in the time domain during the simulation operation test of points A7∼A8.

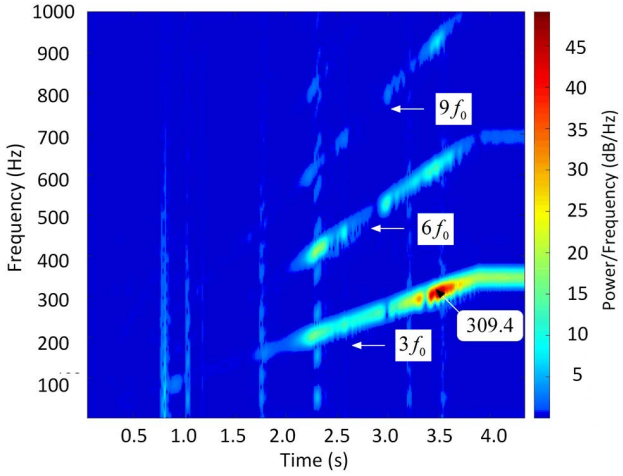

FIGURE 34. Time-frequency diagram of the simulation operation test.

RMS values of points A1∼A6 are 12.87 g, 18.56 g, 11.80 g, 18.48 g, 16.77 g and 14.59 g, respectively. Moreover, by comparing the simulation results in Figure 15. with the measured results in Figure 31 and Figure 32, it can be seen that the structural dynamics model constructed in this paper can basically reproduce the measured results. Thus, the effectiveness of this model has been verified.

Figure 33 shows the acceleration response and RMS values of points A7∼A8. The RMS values of the acceleration response of the outer cryostat (A8) and the cold head (A7) are 10.25 g and 3.06 g, respectively. There is also no structural damage. Figure 34 shows the time-frequency diagram of point A1 during the simulated operation test. Compared with the measured results in Figure 30, the amplitude of each signal increases significantly, and the 50 Hz constant frequency is not displayed because of its relatively weak signal amplitude. Moreover, there are many shock signals, as shown by the highlighted vertical lines. The shock signals might be caused by the collision between the fixed device and other fixed components. No quenching phenomenon was observed during the test. Therefore, the HTS mover magnet has good vibration adaptability, and both the proposed design and fabrication method were confirmed.

VI. CONCLUSION

A coated superconductor magnet serving as the mover magnet of an HTS-LSM has been designed, fabricated and tested. It was proven that the magnet can be cooled to below 23 K with an excitation current of 246 A, and it can operate stably under the vibration environment of 18 gRMS without any quenching and structural damage observed. The following conclusions were drawn.

(i) The proposed epoxy impregnation method using Araldite MY750 epoxy resin to fabricate HTS coils insulated by single-side PTFE was verified by static and dynamic tests. The method can improve the thermal coupling of HTS coils used in a dynamic environment.

(ii) The thermal design of the PCS has a great influence on the temperature rise of the HTS magnet. The PCS should be insulated from the coil case to prevent an excessive temperature rise of the HTS mover coil during the PCS heating. More work should be done about the optimization of the PCS cooling path considering the balance between opening–closing time and magnet temperature rise.

(iii) The established thermal model and structural dynamics model can basically reproduce the temperature variation in the cooling process and the acceleration response caused by the electromagnetic force of the magnet. It provides important tools for static and dynamic performance analysis of HTS magnets.

(iv) The proposed off-line simulation method can realize the evaluation of the actual operation dynamic characteristics of the HTS-LSM with lower cost and shorter test time. In the 400 m/h simulated propulsion test, the HTS mover magnet was not quenched with a vibration acceleration of 18 gRMS, and the cool head was not damaged with a vibration acceleration of 3 gRMS.

Ultimately, the design method, analysis model, manufacturing process and off-line simulation test method of the HTS magnet serving as the HTS-LSM mover have been verified based on the static and dynamic experimental results. The magnet is capable of being stably operated at 246 A under a vibration environment of 18 gRMS. In the future, research on the optimization of the PCS cooling conduction structure and superconducting joint will be carried out.

REFERENCES

[1] K. Mizuno, M. Sugino, M. Tanaka, and M. Ogata, "Development of a real-scale REBCO coil for the demonstration of a magnetomotive force of 700 kA," *Quart. Rep. RTRI*, vol. 58, no. 4, pp. 318–323, 2017.

[2] H. S. Han and D. S. Kim, "Magnetic levitation," in *Maglev technology and applications* (Springer Tracts on Transportation and Traffic), vol. 13. Berlin, Germany: Springer, 2016.

[3] H. Nakao, T. Yamashita, Y. Sanada, M. Yamaji, S. Nakagaki, T. Shudo, M. Takahashi, A. Miura, M. Terai, M. Igarashi, T. Kurihara, K. Tomioka, and M. Yamaguchi, "Development of a modified superconducting magnet for maglev vehicles," *IEEE Trans. Appiled Supercond.*, vol. 9, no. 2, pp. 1000–1003, Jun. 1999.

[4] E. Suzuki, "Heating phenomena in the superconducting magnet of a maglev vehicle caused by electromagnetic vibration," *Cryogenics*, vol. 37, no. 7, pp. 363–370, Jul. 1997.
[5] M. Ogata, T. Okino, K. Ikeda, T. Herai, M. Igarashi, and T. Furusawa, "Vibration characteristics of superconducting magnets for the Yamanashi maglev test line vehicles," *Quart. Rep. RTRI*, vol. 41, no. 2, pp. 79–82, 2000.
[6] M. Iwamatsu, M. Ogata, H. Seino, T. Herai, and T. Asahara, "Development of superconducting magnet for simplified ground coils," *Quart. Rep. RTRI*, vol. 47, no. 1, pp. 12–17, 2006.
[7] K. Mizuno, M. Ogata, and H. Hasegawa, "Manufacturing of REBCO coils strongly bonded to cooling members with epoxy resin aimed at its application to maglev," *Phys. C, Supercond. Appl.*, vol. 506, pp. 138–142, Nov. 2014.
[8] K. Mizuno, M. Ogata, and H. Hasegawa, "Manufacturing of a REBCO racetrack coil using thermoplastic resin aiming at maglev application," *Phys. C, Supercond. Appl.*, vol. 518, pp. 101–105, Nov. 2015.
[9] K. Mizuno, M. Sugino, M. Tanaka, and M. Ogata, "Experimental production of a real-scale REBCO magnet aimed at its application to maglev," *IEEE Trans. Appl. Supercond.*, vol. 27, no. 4, pp. 1–5, Jun. 2017.
[10] K. Mizuno, M. Tanaka, and M. Ogata, "Mechanical vibration tests on real-scale REBCO coil," *QR RTRI*, vol. 59, no. 4, pp. 287–292, Nov. 2018.
[11] K. Mizuno, M. Tanaka, and M. Ogata, "Evaluation of eddy current heating in a REBCO magnet due to the magnetic field of ground coils for the maglev," *Supercond. Sci. Technol.*, vol. 33, no. 7, Jul. 2020, Art. no. 074009.
[12] W.-S. Kim, S.-Y. Jung, H.-Y. Choi, H.-K. Jung, J. H. Kim, and S.-Y. Hahn, "Development of a superconductingl inear synchronous motor," *IEEE Trans. Appl. Supercond.*, vol. 12, no. 1, pp. 842–845, Mar. 2002.
[13] C.-Y. Lee, J.-H. Lee, J. Lim, S. Choi, J.-M. Jo, K.-S. Lee, Y. D. Chung, S. Kim, and H. Lee, "Design and evaluation of prototype high-T_c superconducting linear synchronous motor for high-speed transportation," *IEEE Trans. Appl. Supercond.*, vol. 30, no. 4, pp. 1–5, Jun. 2020.
[14] C. Y. Lee, J. Lee, J. H. Lee, J. M. Jo, C. B. Park, W. H. Rue, Y. D. Chung, Y. J. Hwang, T. K. Ko, and S.-Y. Oh, "Conceptual design of superconducting linear synchronous motor for 600-km/h wheel-type railway," *IEEE Trans. Appl. Supercond.*, vol. 24, no. 3, pp. 1–4, Jun. 2014.
[15] J. K. Noland, "Prospects and challenges of the hyperloop transportation system: A systematic technology review," *IEEE Access*, vol. 9, pp. 28439–28458, 2021.
[16] S. Y. Choi, C. Y. Lee, J. M. Jo, J. H. Choe, Y. J. Oh, K. S. Lee, and J. Y. Lim, "Sub-sonic linear synchronous motors using superconducting magnets for the hyperloop," *Energies*, vol. 12, no. 24, p. 4611, Dec. 2019.
[17] G. Ma, T. Gong, H. Zhang, Z. Wang, X. Li, C. Yang, K. Liu, and W. Zhang, "Experiment and simulation of REBCO conductor coils for an HTS linear synchronous motor," *IEEE Trans. Appl. Supercond.*, vol. 27, no. 4, pp. 1–5, Jun. 2017.
[18] T. Gong, G. Ma, H. Qian, K. Liu, K. Liu, C. Wang, Z. Zhao, and W. Zhang, "Electromagnetic investigation of a high-temperature superconducting linear synchronous motor for high-speed railway," *IEEE Trans. Appl. Supercond.*, vol. 28, no. 3, pp. 1–5, Apr. 2018.
[19] G. Ma, T. Gong, R. Wang, S. Li, X. Nie, P. Zhou, J. Li, C. Li, Z. Ge, and H. Cui, "Design, fabrication and testing of a coated conductor magnet for electrodynamic suspension," *Supercond. Sci. Technol.*, vol. 35, no. 2, Feb. 2022, Art. no. 025013.
[20] F. Dong, Z. Huang, L. Hao, X. Xu, Z. Jin, and N. Shao, "An on-board 2G HTS magnets system with cooling-power-free and persistent-current operation for ultrahigh speed superconducting maglevs," *Sci. Rep.*, vol. 9, no. 1, pp. 1–12, Aug. 2019.
[21] F. Dong, Z. Huang, X. Xu, L. Hao, N. Shao, and Z. Jin, "Improvement of magnetic and cryogenic energy preservation performances in a feeding-power-free superconducting magnet system for maglevs," *Energy*, vol. 190, Jan. 2020, Art. no. 116403.
[22] Z. Huang, F. Dong, X. Xu, X. Teng, W. Ren, J. Zhang, W. Li, G. Ma, and Z. Jin, "Evaluation of the structural dynamics of a 2G HTS magnet system considering electromagnetic and thermal stress," *IEEE Trans. Appl. Supercond.*, vol. 31, no. 5, pp. 1–5, Aug. 2021.
[23] Z. Huang, F. Dong, X. Xu, X. Teng, W. Ren, J. Zhang, W. Li, G. Ma, and Z. Jin, "Comparison of long stator three-phase winding structures in a 2G HTS LSM for maglev application," *IEEE Trans. Appl. Supercond.*, vol. 31, no. 5, pp. 1–5, Aug. 2021.
[24] X. Teng, Z. Huang, F. Dong, X. Xu, Z. Jin, Y. Shi, A. Zhao, X. Yuan, and Y. Feng, "Design and key performance of 2G HTS coils for high speed superconducting maglev application," *IEEE Trans. Appl. Supercond.*, vol. 31, no. 5, pp. 1–5, Aug. 2021.
[25] Y. Iwasa, *Case Studies in Superconducting Magnet*, 2nd ed. Berlin, Germany: Springer, 2009.
[26] H.-M. Chang and S. W. Van Sciver, "Thermodynamic optimization of conduction-cooled HTS current leads," *Cryogenics*, vol. 38, no. 7, pp. 729–736, Jul. 1998.

DAOYU HU received the B.S. degree in electrical engineering from Zhejiang University, Zhejiang, in 2013, and the Ph.D. degree in electrical engineering from Shanghai Jiao Tong University, Shanghai, in 2018. He is currently a Senior Engineer with the Institute of Magnetic Levitation and Electric Propulsion, China Aerospace Science and Technology Research Institute, China. His research interests include design, analysis and manufacturing of superconducting electrodynamic suspension, eddy-current brake, and linear motor.

YI ZHANG received the B.S. and Ph.D. degrees in electrical engineering from the Huazhong University of Science and Technology, Wuhan, China, in 2010 and 2019, respectively. He is currently a Middle Engineer with the Institute of Magnetic Levitation and Electric Propulsion, China Aerospace Science and Technology Research Institute, China. His research interests include design, analysis, and manufacturing of high-temperature superconducting magnet.

KAI MAO received the B.S. and M.E. degrees in electrical engineering from Harbin Industrial University, Harbin, China, in 2003 and 2005, respectively. He is currently the Director of the Institute of Magnetic Levitation and Electric Propulsion, China Aerospace Science and Technology Research Institute, China. He is leading the research team to develop the ultra-high speed and low vacuum pipeline maglev train using superconducting technology.